International Journal of Heat and Mass Transfer 177 (2021) 121526

Contents lists available at ScienceDirect

International Journal of Heat and Mass Transfer

journal homepage: www.elsevier.com/locate/hmt

Enhancement of vapor condensation heat transfer on the micro- and nano-structured superhydrophobic surfaces

Xin Wang[a], Bo Xu[a,*], Qiusheng Liu[d], Yang Yang[e], Zhenqian Chen[a,b,c,*]

[a] School of Energy and Environment, Southeast University, Nanjing, China
[b] Key Laboratory of Energy Thermal Conversion and Control of Ministry of Education, School of Energy and Environment, Southeast University, Nanjing, China
[c] Jiangsu Provincial Key Laboratory of Solar Energy Science and Technology, School of Energy and Environment, Southeast University, Nanjing, China
[d] Key Laboratory of Microgravity, Institute of Mechanics, Chinese Academy of Sciences, Beijing, China
[e] Engineering and technology center for space applications, Chinese Academy of Sciences, Beijing, China

ARTICLE INFO

Article history:
Received 31 December 2020
Revised 28 April 2021
Accepted 20 May 2021
Available online 6 June 2021

Keywords:
Condensation heat transfer
Micropillar arrays
Lattice Boltzmann method
Droplet dynamics
ESEM

ABSTRACT

Recently, micro- or nano- structured surfaces haven been developed to enhance condensation heat transfer, water harvesting and self-cleaning. However, at large subcoolings, condensate floods the subcooled substrate, thus deteriorating the heat transfer efficiency. Here, the superhydrophobic surfaces with micropillared and nanopillared structures are proposed to enhance heat transfer at large subcoolings. The influence of micropillar spacing and surface subcooling on the droplet dynamics and heat transfer performance is experimentally investigated using microscopic visualization techniques. In addition, the microscopic modeling of condensation heat transfer on the microstructured surfaces is performed using the mesoscopic lattice Boltzmann method. The results demonstrate that the droplet size distribution on the micropillared surface is significantly smaller over that of the nanostructured surface. The heat transfer coefficient decreases with the increase of micropillar spacing. As the subcooling rises, although the condensate floods the substrate, the heat transfer coefficient of the S10R30 (S10R30 represents the micropillar arrays with $s = 10\ \mu$m and $2r = 60\ \mu$m) surface is enhanced by 26.4% compared to the hydrophobic nanostructured surface. This is because the height of liquid film is the same of order of magnitude as the micropillars, reducing the thermal resistance caused by the liquid layer. Combining environmental scanning electron microscope (ESEM) observations and LB simulation results, it is concluded that the droplets first nucleate at the bottom corner of micropillars. In addition, the condensate droplets merge to form a film, fill the micropillar gaps, and cover the entire micropillars, leading to a sharp decrease in heat flux. These findings provide a theoretical and experimental guidance for the development of condensing surfaces to enhance heat transfer.

© 2021 Elsevier Ltd. All rights reserved.

1. Introduction

Heterogeneous condensation is essential in the numerous industrial processes, involving from thermal management of small-scale high-power electronics to the cooling of large-scale power plant [1,2]. In addition, it has great potential value in water harvesting [3–5], anti-icing / defrosting [6] and Heating, Ventilation and Air Conditioning (HVAC) [7]. It is well-known that the surface morphology and wettability of condensing surfaces are significant for the condensation modes (dropwise or filmwise condensation). In the current industrial applications, filmwise condensation has been widely applied, whereas this heat transfer mechanism provides the extremely lower heat transfer efficiency due to the thermal resistance of liquid layer [8,9]. Compared to the conventional filmwise condensation, dropwise condensation on the superhydrophobic surfaces (SHS) with micro- and nano-structures has inherent advantages, such as high-frequency droplet removal, low interfacial thermal resistance and superior heat transfer efficiency, and is expected to be an efficient means of phase-change heat transfer in industrial engineering.

Over the past decade, a large number of researchers have concentrated on the design and fabrication of advanced functional surfaces including bionic micropatterns [10–14], oxidized nanostructured surfaces [15–19] and microstructured pillars [20–24] to reduce the critical departure size of condensate droplets and enhance condensation heat transfer. Excitingly, several interesting dynamic behaviors of drops were observed on these special surfaces,

* Corresponding author.
E-mail addresses: xubo@seu.edu.cn (B. Xu), zqchen@seu.edu.cn (Z. Chen).

https://doi.org/10.1016/j.ijheatmasstransfer.2021.121526
0017-9310/© 2021 Elsevier Ltd. All rights reserved.

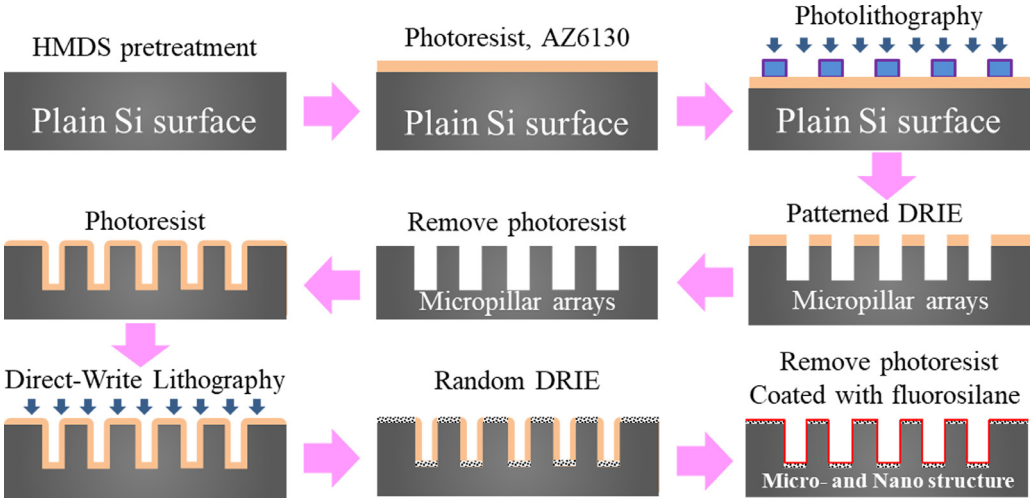

Fig. 1. Dry etching technology for preparing the silicon surfaces with two-layer micro- and nano-structures.

such as self-propelled jumping [25–27], spontaneous dewetting [28] and directional migration [12]. Boreyko and Chen [25] first reported the self-propelled jumping of condensate droplets on the SHS due to the release of excess surface energy by coalesced droplets. Subsequently, many efforts have been devoted to optimizing the surface structure to strengthen the jumping ability of condensate droplets and enhance condensation heat transfer. Mulroe et al. [26] investigated the relationship between critical jumping size and the substrate nanostructures and concluded that slender and elongated nanopillars greatly promoted the smaller droplet jumping (~2 μm). Wen et al. [27] fabricated the 3D nanowire SHS to maintain the stable droplet jumping condensation at a larger surface subcooling (~28 K). Unfortunately, the excessive nucleation of nanodroplets in the nanostructured gaps leads to the irreversible wetting transition from Cassie state to Wenzel state at large subcoolings, which significantly deteriorates the heat transfer efficiency [29,30]. Although the coalescence-induced self-propelled jumping of condensate droplets at the lower subcooling on the various functional surfaces has been extensively studied, the droplet dynamics and heat transfer performance on the micro- and nanostructured SHS at the larger surface subcooling have not attracted sufficient attention. Orejon et al. [31] carried out the simultaneous filmwise and dropwise condensation on the hydrophilic micropillared surfaces and demonstrated a better heat transfer efficiency over the conventional filmwise condensation. However, the heat transfer performance of simultaneous filmwise and dropwise condensation is lower than the dropwise condensation on the SHS. Therefore, it is necessary to further investigate the condensation on the microstructured SHS to enhance heat transfer performance.

Note that, the current experimental studies of condensation have focused on the dynamic behaviors of condensate droplets via high-speed camera or environmental scanning electron microscopy (ESEM), and the heat transfer performance obtained by Fourier's law [15,29–32]. However, the microscopic dynamic evolution of droplets and its influence on the heat transfer performance is still unclear due to the limitations of experimental equipment (e.g. low capture rates of ESEM). Due to the advantages of natural parallel efficiency and dealing with complex boundaries [33,34], the mesoscopic lattice Boltzmann (LB) method is adopted to model the condensation heat transfer and reveal the microscopic mechanisms of vapor condensation on the microstructured surfaces. LB mesoscopic simulations play a ground-breaking role in understanding the complex mechanism of condensation heat transfer. For the first time, Liu and Cheng [35] successfully simulated the laminar filmwise condensation on the vertical plates using the LB method. Subsequently, dropwise condensation and transition from dropwise to filmwise condensation were simulated by their team [36–38]. In addition, the effect of non-condensable gasses was also considered [39,40]. However, the influence of micropillar on the condensate dynamics and heat transfer is neglected.

This work aims to observe the dynamic evolution of condensate droplets on the micropillared surfaces via the microscopic visualization technology. In the meantime, the multiphase LB method is adopted to model the condensation heat transfer. The effects of micropillar and surface subcooling on the droplet dynamics and heat transfer performance are investigated in microscale. It will further contribute to the potential applications of condensation heat transfer in power plants, water harvesting, and thermal management of electronics.

2. Experimental setup

2.1. Surface fabrication

The silicon surfaces with two-layer micro- and nano-structures are fabricated by dry etching technology, as shown in Fig. 1. Firstly, HDMS is coated on a flat silicon plate with $r = 20$ mm to enhance the surface adhesion. Then, the photoresist (AZ6130) is evenly deposited on the silicon surface and baked at 100 °C for 2 min. After 4.5 s of exposure to UV light, the sample is exposed to the developer (3038) for 45 s. The photoresist is hardened at 110 °C for 2 min and treated as a mask for the deep reaction ion etching process. Standard photolithography technique is used to etch micropillars with a height of 25 ± 1 μm. The micropillared silicon sample is uniformly sprayed with the 2 μm thick photoresist again. Nanostructures with the height of 1 ± 0.3 μm are randomly etched out by a direct-write lithograph. Then, the sample is cleaned in the acetone and isopropanol solution. However, silicon wafers are hydrophilic. To enable a superhydrophobic silicon surface with micropillars and nanostructures, the hydrophobic fluorosilane coatings ($\theta = 114.0°$) are also required to cover the substrates. The silicon samples are soaked in the 0.1wt% ethanol solution of 1H, 1H, 2H, 2H-perfluorodecyltriethoxysilane (Aladdin, AR) by 1 h at the room temperature and then dried by nitrogen gas. Eventually, a superhydrophobic silicon surface with two-layer micro- and nanostructures can be successfully obtained.

Twelve micropillared samples with different width and spacing are fabricated by dry etching, with width of $2r = 20$ μm and $2r = 60$ μm, and spacing of $s = 10$ μm, $s = 20$ μm, $s = 30$ μm, $s = 40$ μm, $s = 50$ μm and $s = 60$ μm. In the experiments, the

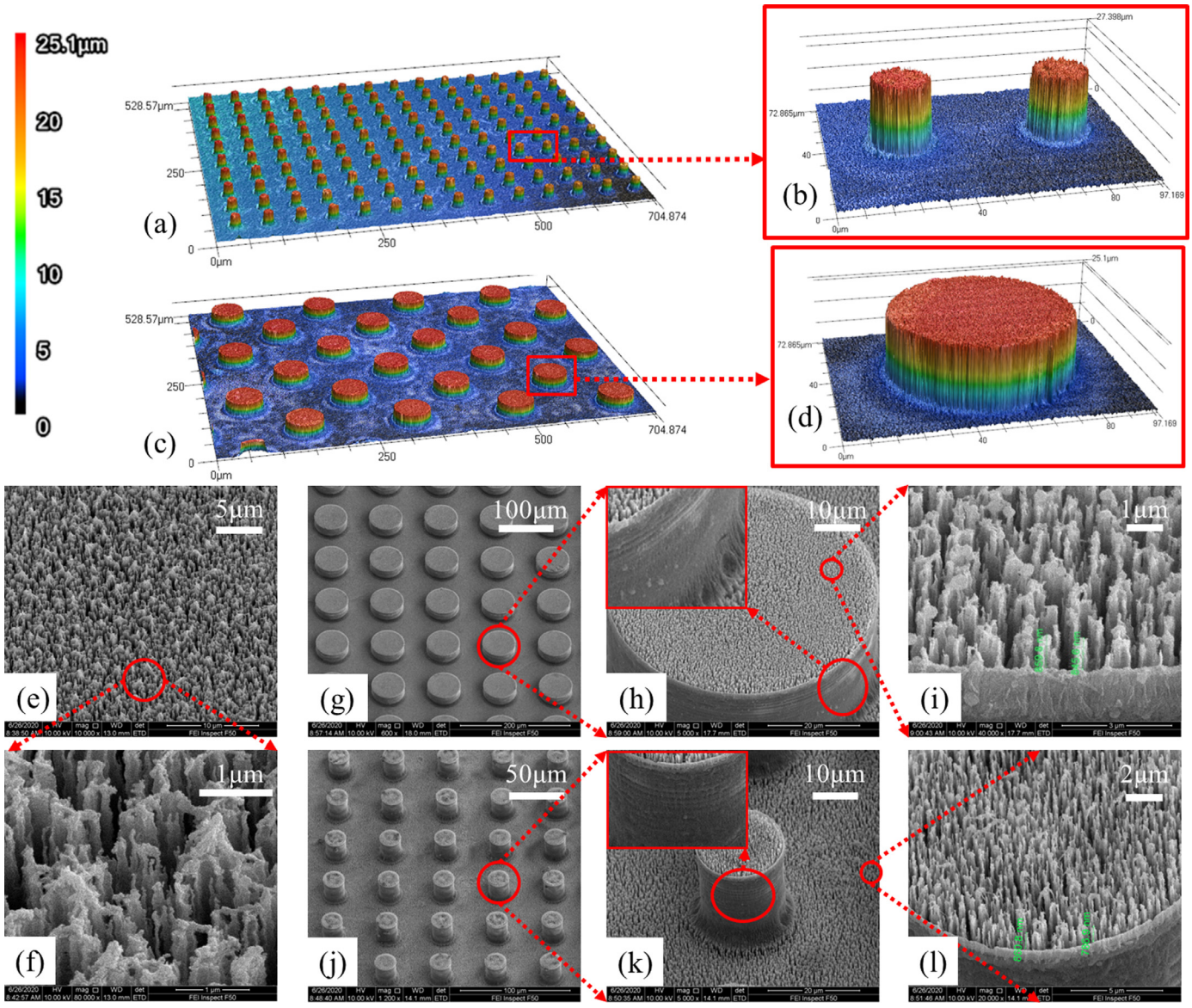

Fig. 2. Microscopic images of two-layer micro- and nano-structured silicon surfaces.

height of micropillars is the same with 25 μm to reduce the thermal resistance exerted by the condensate droplets between micropillars. Figs. 2(a-d) show the surface morphology characterized by a 3D surface profiler based on scanning white light interferometry. The color ranging from white to red denotes the height of substrate. The width, spacing and height of micropillar arrays can be clearly seen. It should be noted that the fabrication of micropillar arrays by dry etching method result in a tiny error of $\pm$1.0 μm. In addition, nanopillar arrays with the height of about 1.0 $\pm$ 0.3 μm are added at the top of micropillars. Besides, there exists an error of $\pm$0.1 μm in 3D surface profiler based on scanning white light interferometry. It means that the height of the micropillar arrays covered with nanopillars ranges from 24.6 μm to 27.4 μm. However, the nanostructures cannot be observed by the 3D surface profiler. Figs. 2(e-l) give the field emission scanning electron microscope (FESEM) images of the silicon sample with three different surfaces: nanostructured surface in Figs. 2(e, f), micropillared surface with $2r = 60$ μm and $s = 40$ μm in Figs. 2(g-i) and micropillared surface with $2r = 20$ μm and $s = 30$ μm in Figs. 2(j-l). A dense layer of nanostructures exist at the top and bottom of micropillar arrays while the side of micropillars is smooth without nanostructures.

2.2. Experimental setup

In order to study the dynamic evolution of condensate droplets and heat transfer performance on the microstructured surfaces, a self-constructed visualization platform was built and pure steam condensation heat transfer experiments were conducted in a closed system, as shown in Fig. 3. It is composed of a steam generator, condensing chamber, post-condenser, cooling water system and data acquisition system. All experiments are performed at a saturated pressure of 47.6 $\pm$ 0.1 kPa and a saturated temperature of 80 $\pm$ 0.5 °C. Microscopic visualization experiments of dropwise condensation on the vertically oriented surfaces are performed in a custom stainless steel (310S) condensing chamber, as shown in Fig. 3(a). During the condensation, the required pure saturated steam is supplied by the steam generator and enters through the upper of condensing chamber. The cooling system is used to absorb the heat released by steam and control the temperature of condensing surface by adjusting the temperature of the water bath.

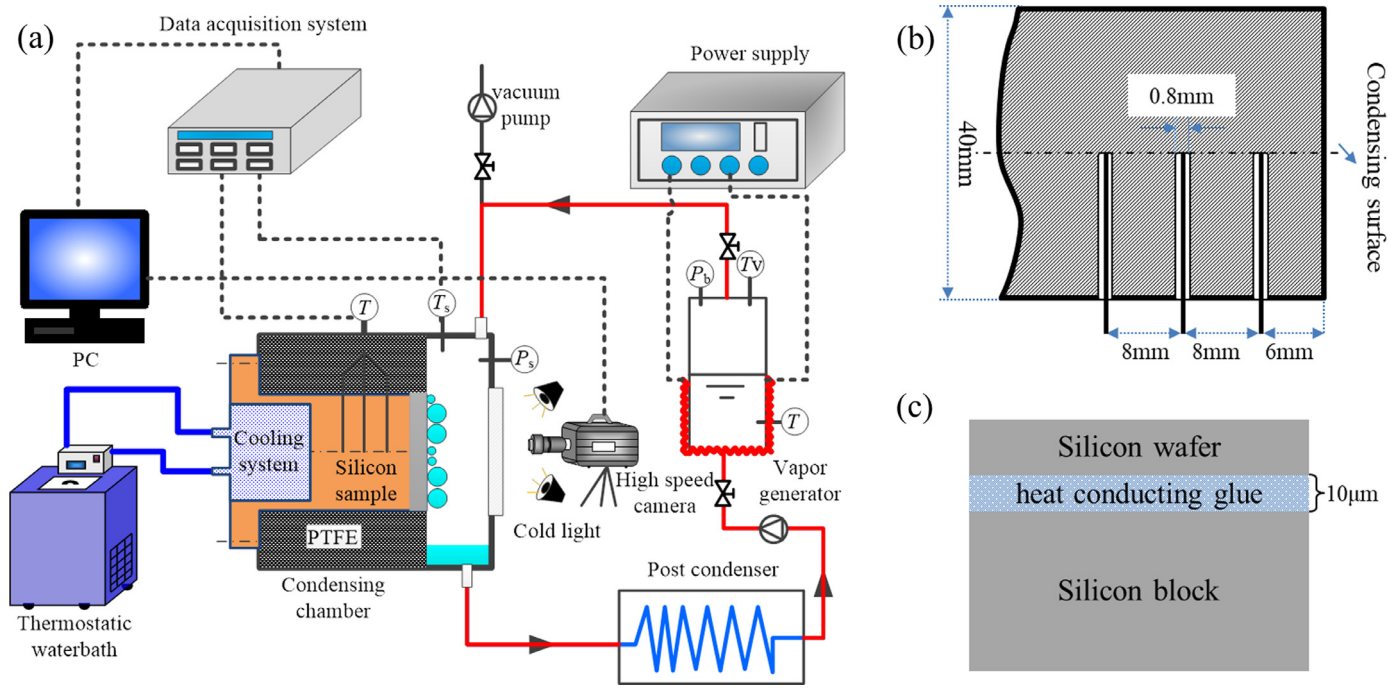

Fig. 3. Schematic of experimental setup.

Along the axis of the silicon block, three K-type thermocouples are penetrated to the centreline at a depth of 20.0 mm. The distances from the first thermocouple T_1 to the condensing surface, from T_1 to T_2, and from T_2 to T_3 are 6.0 mm, 8.0 and 8.0, respectively (Fig. 3b). The heat conducting glue (5.2 W/m•K^{-1}, Dow Corning, TC-5888) is filled between the thermocouples and the drilling holes. An extremely thin layer of thermally conductive silicone grease (~10 μm thickness) is coated between the micro- and nano-structured substrate and the silicon block (Fig. 3c). The steam condenses on the silicon substrate, and the accumulated condensate is discharged pipes at the bottom of the chamber to the reservoir. To prevent the excess heat release into the chamber, the sides of silicon block are tightly wrapped with a 10.0 mm thick Teflon (PTFE) insulation. The right side of the chamber is equipped with a transparent glass window for observing the droplet dynamics using a high-speed camera. The temperature and pressure in the condensing chamber are measured by the K-type thermocouples and the pressure gauges, respectively. All relevant pressures and temperatures are recorded by a data acquisition system.

In order to eliminate the influence of non-condensable gas on the dropwise condensation, the non-condensable gas in the whole system must be discharged before carrying out the experiment. Firstly, the pressure in the loop was decreased to the saturated pressure corresponding to the room temperature by a vacuum pump. Then, the steam generator was heated continuously with a high power for 1 h to remove the accumulated non-condensable gas. Finally, the pressure in the loop was pumped to less than 20.0 Pa, without leakage within 24 h. In addition, the leak rate in the chamber was checked before each run to ensure the pure steam condensation.

2.3. Data reduction

For any testing surface, the heat flux can be varied by adjusting the temperature of the water bath. The condensation heat flux q is obtained according to the three thermocouples, assuming one-dimensional thermal conductivity of the cylinder silicon block. The relationship between T_1, T_2 and T_3 (i.e., the temperature difference from T_1 to T_2 and from T_2 to T_3) is examined to determine if one-dimensional heat transfer is satisfied. The experimental results indicate that the values of T_1-T_2 and T_2-T_3 are nearly the same in each test (See Fig. S1). Therefore, the axial thermal conductivity of the silicon block is negligible to ensure a radial one-dimensional heat transfer. The heat flux q can be calculated as $q = \frac{\lambda}{L_{1-3}}(T_1 - T_3)$, where the thermal conductivity of silicon is 148 W/m•K^{-1}. Due to the extremely thin thickness of thermally conductive silicone grease between the silicon block and the condensing sample, the additional thermal resistance caused by the thermally conductive silicone grease is ignored. The condensing wall temperature, T_w, is obtained by extending the axial linear temperature distribution of the silicon block to the location of the condensing surface. The surface subcooling is defined as $\Delta T = T_s - T_w$, where T_s is the temperature of saturated steam. The condensation heat transfer coefficient (HTC) h_c is expressed as $h_c = \frac{q}{\Delta T} = \frac{q}{(T_s - T_w)}$. In view of Moffat's method [41], the uncertainty analysis of experimental data was performed as follows: $\delta R = [\sum_{i=1}^{N} (\frac{\partial R}{\partial V_i}\delta V_i)^2]^{1/2}$. where δ_R denotes the uncertainty of any experimental data R, which depends on a series of measured parameters V_i. And δV_i is the uncertainty of the measured data V_i. As shown in Table 1, the uncertainties of measured and experimental data are collected and calculated, respectively.

Table 1
Uncertainties of several measured and calculated variables.

Parameters	Uncertainties
Micropillar size 2r, s, h	±1μm
Temperature T_1, T_2, T_3, T_s	±0.5 °C
Vapor pressure P	±0.25%
Contact angle θ	±0.1°
Droplet diameter d	±10μm
Heat flux q	±6.83%
Heat transfer coefficient h_c	±9.01%

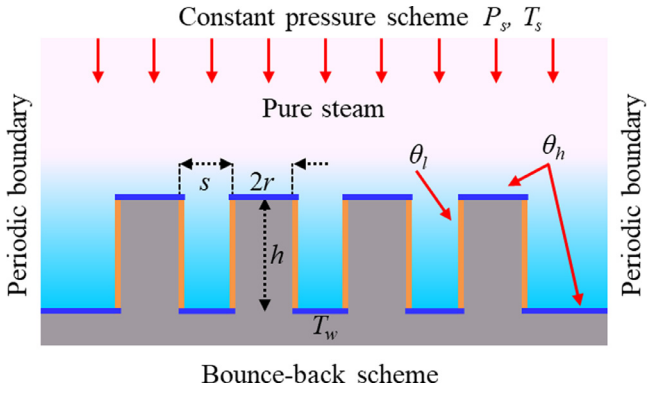

Fig. 4. Schematic of dropwise condensation on the micropillared surface.

3. Numerical method

The single-component multiphase mesoscopic LB method is adopted to model the flow field of steam condensation, and the temperature equation is discretized using a finite difference method to solve the temperature field, which further explores the influence of micropillared structure on the droplet dynamics and heat transfer performance [42,43]. In the pseudopotential model, the fluid migration and collision is described by a specific particle distribution function. Using the multi-relaxation-time collision operator [44], the density distribution equation used to describe the particle evolution is:

$$f_i(\mathbf{x}+\mathbf{e}_i\delta_t, t+\delta_t) - f_i(\mathbf{x},t) = -\left(\mathbf{M}^{-1}\mathbf{\Lambda}M\right)\left[f_i - f_i^{eq}\right] + \mathbf{F}_i'\delta_t \quad (1)$$

where $f_i(\mathbf{x},t)$ denotes the density distribution function along the i^{th} direction at time t and position $\mathbf{x}$. In the D2Q9 model, the discrete velocity is written as:

$$[\mathbf{e}_0,\mathbf{e}_1,\mathbf{e}_2,\mathbf{e}_3,\mathbf{e}_4,\mathbf{e}_5,\mathbf{e}_6,\mathbf{e}_7,\mathbf{e}_8] = c\cdot\begin{bmatrix}0 & 1 & 0 & -1 & 0 & 1 & -1 & -1 & 1\\ 0 & 0 & 1 & 0 & -1 & 1 & 1 & -1 & -1\end{bmatrix} \quad (2)$$

$\mathbf{F}_i'$ is the force term in the discrete velocity space. The force term is added to the right side of Eq. (1) using the exact difference method. Generally, the force term is composed of the fluid-fluid force, fluid-solid force and gravitational force. To achieve the separation of the gas and liquid phases, it is necessary to introduce a non-ideal gas equation of state. Here, Peng-Robinson (P-R) equation is chosen [45]:

$$p = \frac{\rho RT}{1-b\rho} - \frac{a\rho^2\alpha(T)}{1+2b\rho-b^2\rho^2} \quad (3)$$

The detailed information of LB model can be seen in our previous work [46]. Fig. 4 shows a schematic diagram of the dropwise condensation on the micropillared surface. The constant pressure boundary proposed by Zou-He [47] is applied at the upper boundary, and the bounce-back scheme is adopted at the bottom boundary. Periodic boundary conditions are used for the other boundaries. The temperature boundaries are set as follows: adiabatic boundary applied at the left and right boundary, $T = T_s$ at the upper boundary to ensure saturated steam entering the system and $T = T_w = 0.78T_s$ at the bottom boundary. The density ratio is 17.1 approximately with the coexistence densities $\rho_l = 6.5$ and $\rho_v = 0.38$ at the saturated temperature (T_s) in lattice units. All LB simulations of vapor condensation are performed at the same operating condition. The contact angle at the side of micropillars (θ_l) is lower than that at the top and the top of micropillars (θ_h), which is in agreement with the silicon sample in experiments.

4. Results and discussion

4.1. Contact angle

To begin with, the effects of micropillar spacing and width on the apparent contact angle are investigated. The apparent contact angle of single droplet is measured by a contact angle measuring instrument (KRUSS DSA25). As shown in Fig. 5(a), the apparent contact angle of a droplet with $R = 776$ μm on the microstructured surface is 135.2°. The nanostructures, illustrated in Fig. 2(g), between the droplet and silicon sample determine the wettability of substrate. In contrast, the apparent contact angle of droplet is significantly increased by adding the micropillar arrays to the substrate. For example, the contact angle of droplet on the micropillared surface with $2r = 30$ μm, $s = 40$ μm, and $h = 25$ μm is 155.9° Furthermore, an enlarged image of the bottom of the droplet in contact with the substrate shows that several white spots in an orderly arrangement between the droplet and the substrate, indicating that the droplet is suspended on the microstructured surface in the Cassie state rather than impaled Wenzel state. Cassie and Baxter [48] reported that, when the droplet is suspended on the surface, the relationship between the apparent contact angle and the microstructure is expressed as:

$$\cos\theta_c = -1 + \phi_s(1+\cos\theta_e) \quad (4)$$

where ϕ_s represents the solid fraction of substrate, $\phi_s = \frac{\pi r^2}{(s+2r)^2}$. Fig. 5(e) shows the three-dimensional schematic of the micropillared surface. The letters $2r$, s and h represent the width, spacing, and height of micropillar arrays. Fig. 5(f) plots the variation of apparent contact angle with solid fraction. The gray curve is plotted according to the Cassie-Baxter equation (Eq.4), which demonstrates that the apparent contact angle decreases as the solid fraction increases. The orange dots and pink triangles represent the cylindrical micropillared surface with $2r = 20$ μm and $2r = 60$ μm, respectively. When the solid fraction is greater than 0.2, the experimentally measured apparent contact angle is in good agreement with Cassie-Baxter equation, while it is slightly lower than the theoretical prediction when $\phi_s < 0.2$. This may be due to the larger adhesion force caused by the increased solid-liquid contact area. Overall, the apparent contact angle of droplet agrees well with the Cassie-Baxter equation. In addition, advancing and receding angles of droplets on the micropillared surfaces with different spacing can be seen in Fig. S2.

In addition, 2D numerical simulations of a droplet on the micropillared surface are also performed to verify the applicability of the LB model for simulating condensation heat transfer on the microstructured surface. Nanostructures are neglected in the LB model because of the limitation to grid structure. On a smooth surface, the equilibrium contact angle of a droplet is 135.6° (See Fig. S3), which is almost identical to the apparent contact angle on the nanostructured surface in experiment. After the addition of micropillar arrays, the apparent contact angle of droplet is significantly improved. For example, the apparent contact angle is 150.9° on the surface with $2r = 20$ μm, $s = 20$ μm and $h = 20$ μm (See Fig. S3). Moreover, as the solid fraction increases, the apparent contact angle agrees well with the Cassie-Baxter equation and the experimental results, which further demonstrates the validity of the LB model for simulating condensation heat transfer.

4.2. Effect of micropillar spacing

In order to clearly observe the dynamic behaviors of condensate microdroplets under different condensing conditions, a high-speed camera with a microscopic lens with a minimum resolution of 10 μm is used during the experiment. First, we compare the experimental data of hydrophilic surface with the Nusselt theory.

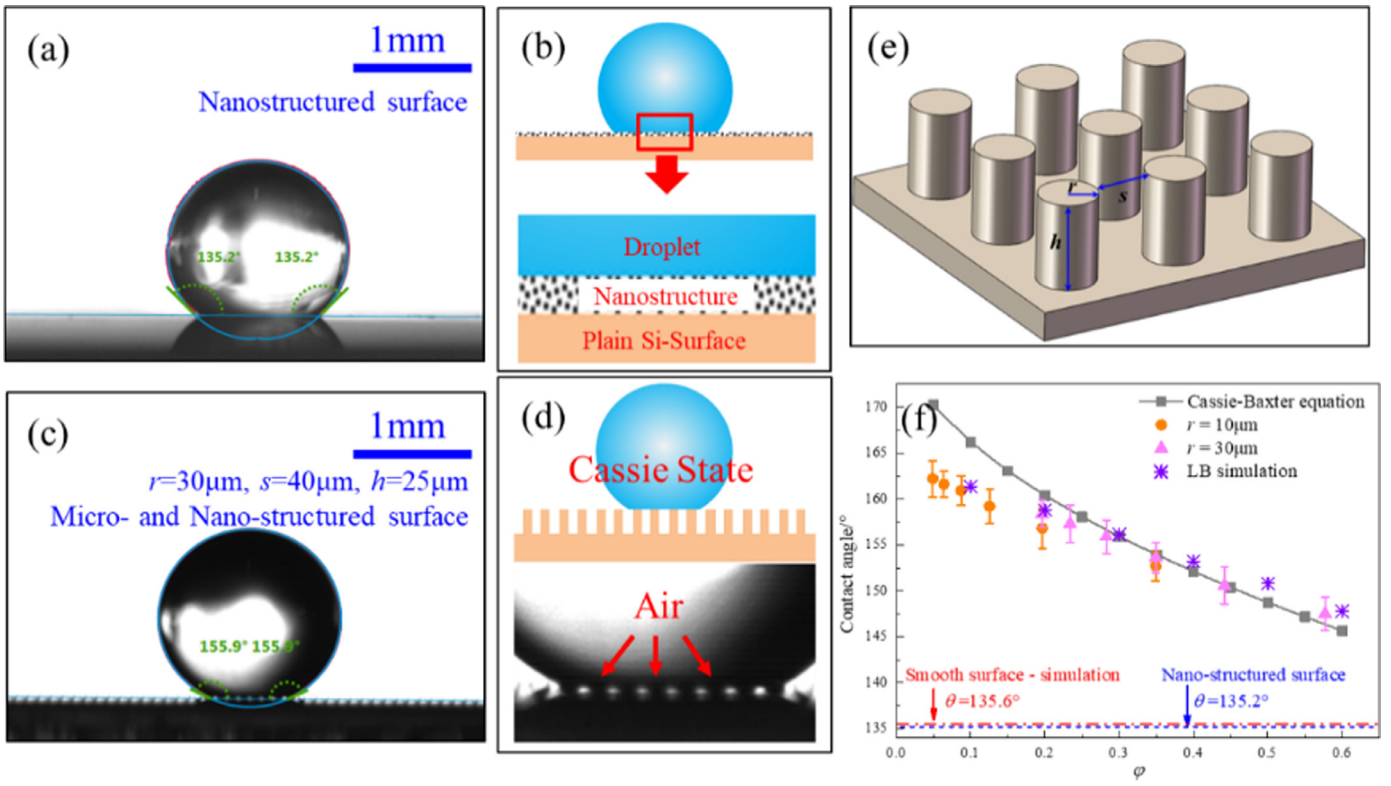

Fig. 5. (a) Apparent contact angles of water droplet on a nanostructured surface, $\theta = 135.2°$; (b) Schematic of droplet on a nanostructured surface; (c) Apparent contact angle of water droplet on a micro- and nano-structured surface with $r = 30$ μm, $s = 40$ μm and $h = 25$ μm, $\theta = 155.9°$; (d) Magnified view of the liquid-solid contact area, showing the air pockets between the micropillars; (e) Schematic of the micropillared surface; (f) Variation of the apparent contact angle with solid fraction. .

Variation of the heat transfer coefficients versus time on the hydrophilic silicon surface at different subcooling degrees agree well with the Nusselt theory, which validates the whole heat transfer measurement system (See Supporting Information S3). Fig. 6 gives the dynamic evolution of condensate droplets on the different nanostructured and micropillared surfaces at a lower surface subcooling ($\Delta T = 1.0$ K). Taking the nanostructured surface (NS) as a reference (Fig. 6a), the condensate droplets present the various irregular shapes. As the condensation proceeds, merging of the droplets can be observed (e.g. droplet 1, 2 and 3; droplet 4 and 5 circled by the red dotted line). The solid-liquid contact area barely changes before and after coalescence, indicating that the condensate droplets penetrate into the nanopillars and are pinned on the substrate with Wenzel state. Finally, the irregularly pinned contact line of a larger droplet is presented at $t = 182.5$ s. For the S10R30 micropillared surface (S10R30 represents the micropillar arrays with $s = 10$ μm and $2r = 60$ μm), the condensate droplets at the valley of pillars grow faster compared to those at the top of pillars. Squeezed by the micropillars, the droplets expand upward after filling the valley. When the bottom droplets grow beyond the height of micropillars, the liquid bridges are formed between the micropillars after coalescence. The droplet in the shape of ellipsoidal (circled in red) is impaled into nanostructures and microstructures at $t = 10.025$ s (Fig. 6b). In the meantime, it can be observed that the droplets at the top pillars also coalesce with each other and grow larger. As the micropillar spacing increases ($s \geq 40$ μm), the growth rate of top droplets at the beginning of condensation is faster than that of bottom droplets, which is different from the S10R30 surface. With the progress of condensation, the droplets at the valley of pillars expand laterally and merge with other droplets to surround the pillars. Eventually, the droplets almost fill the gaps of S40R30 surface at $t = 336.80$ s (Fig. 6c). Some droplets on the S60R30 surface even cover the whole pillars at $t = 164.82$ s, as shown in Fig. 6(d).

Next, the influence of micropillar spacing on the droplet size distribution and heat transfer performance is analysed. For each experimental condition, the condensation experiment is continuously lasted for 40 min, except for the time required to readjust the condensing condition. Limited by the magnification of microscopic lens, the smallest observable droplet size is 10 μm. More than 400 condensate droplets for each condensing condition are counted. Fig. 7(a) plots the droplet size distribution on the different structured surface. For the nanostructured surface as an example, the droplets less than 100 μm account for more than 50% of all droplets. Meanwhile, the proportion of the droplets greater than 500 μm is about 5.7%. Compared to the NS, the proportion of small-sized droplets is larger on the micropillared surface. For the S10R30 surface, the droplets less than 100 μm dominate greatly, exceeding 80%. As the micropillar spacing increases, the smaller droplets at the valley continuously merge with each other, leading to a significant decrease in the proportion of smaller droplets ($d < 100$ μm) but an increase in the proportion of larger droplets (100 μm $< d < 500$ μm). For the S60R30 surface, the droplets between 100 μm and 250 μm are dominant. Fig. 7(b) shows the maximum and average diameter of condensate droplets on the different structured surfaces. The maximum droplet diameter on the nanostructured surface reaches 1126 μm, which is almost one order of magnitude larger than that on the micropillared surface. The maximum droplet size increases with a larger micropillar spacing. And the maximum droplet diameter on the S60R30 surface ($d = 246$ μm) is nearly twice as large as that on the S10R30 surface ($d = 116$ μm). In addition, the average diameter of droplet is reduced by approximately 60% from 96 μm to 38 μm as the micropillar spacing decreases. Fig. 8 shows the variation of condensation heat transfer coefficient with the micropillar spacing. Accord-

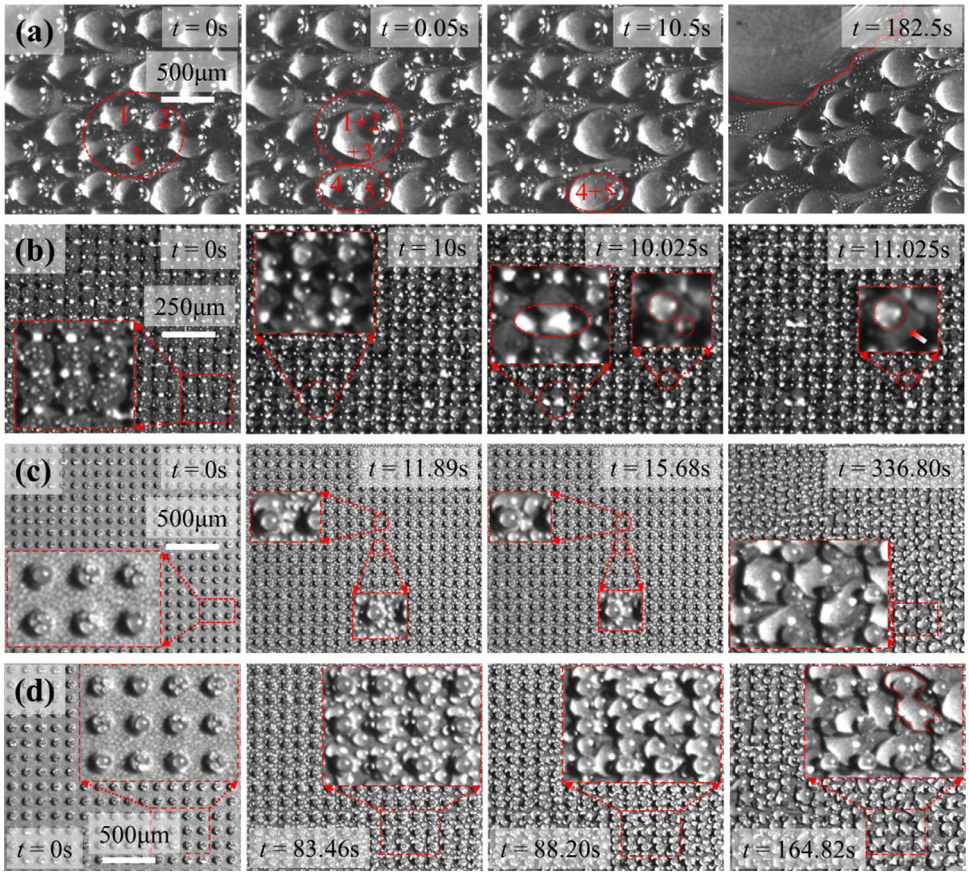

Fig. 6. Dropwise condensation on the subcooled surfaces observed by high-speed camera: (a) Nanostructured surface; Micro- and nano-structured surfaces with (b) $r = 30\ \mu$m, $s = 10\ \mu$m, $h = 25\ \mu$m; (c) $r = 30\ \mu$m, $s = 40\ \mu$m, $h = 25\ \mu$m; and (d) $r = 30\ \mu$m, $s = 60\ \mu$m, $h = 25\ \mu$m. These four condensation experiments are all performed at the subcooling of $\Delta T = 1.0$ K. .

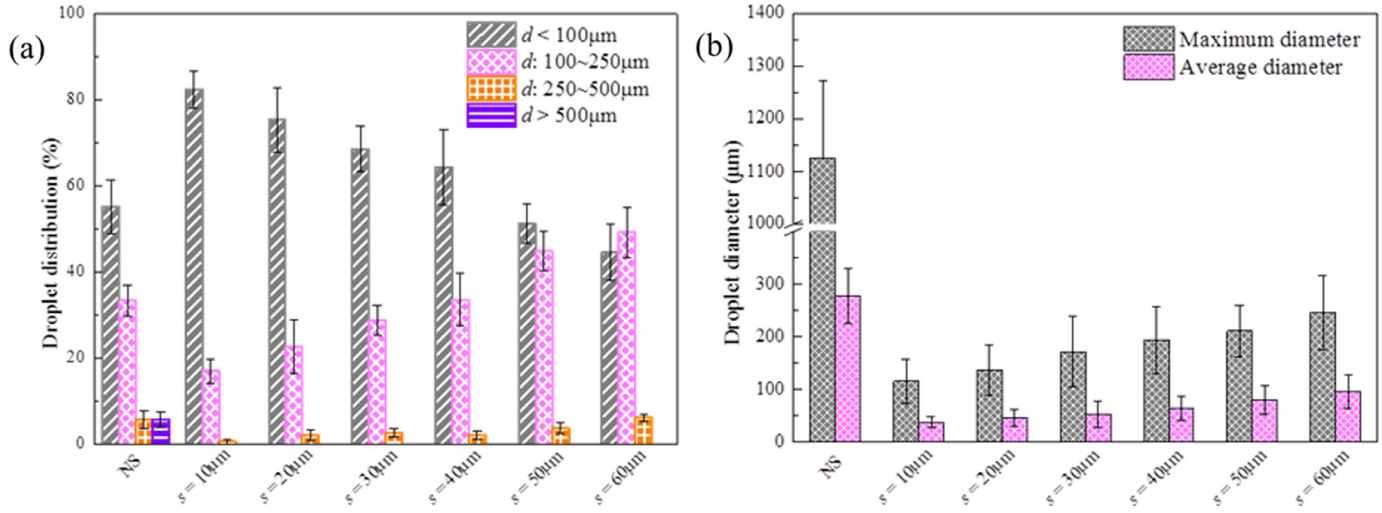

Fig. 7. (a) Droplet size distribution and (b) the maximum and average droplet diameter on the NS and micropillared surfaces with different spacing at 40 min ($\Delta T = 1.0$ K).

ing to the theoretical model of dropwise condensation heat transfer [49], the HTC strongly depends on the droplet size distribution and decreases as the critical departure size increases. it can be concluded that for the same width of micropillars, the HTC decreases with a larger micropillar spacing. Since the maximum and average droplet diameter is increased on a larger micropillared surface, the thermal resistance of liquid layer is larger and heat transfer performance is deteriorated. Comparing the microstructured surfaces with $2r = 20\ \mu$m and $2r = 60\ \mu$m, the results indicate that the HTC of microstructured surface with $2r = 20\ \mu$m is almost the same as that of microstructured surface with $2r = 60\ \mu$m at the same height and spacing.

4.3. Effect of surface subcooling

Steam condensation heat transfer depends not only on the surface microstructure, but also on the surface subcooling. A large number of experimental studies have revealed that a larger subcooling leads to the condensation mode transition from dropwise condensation to filmwise condensation [15,29]. However, the mi-

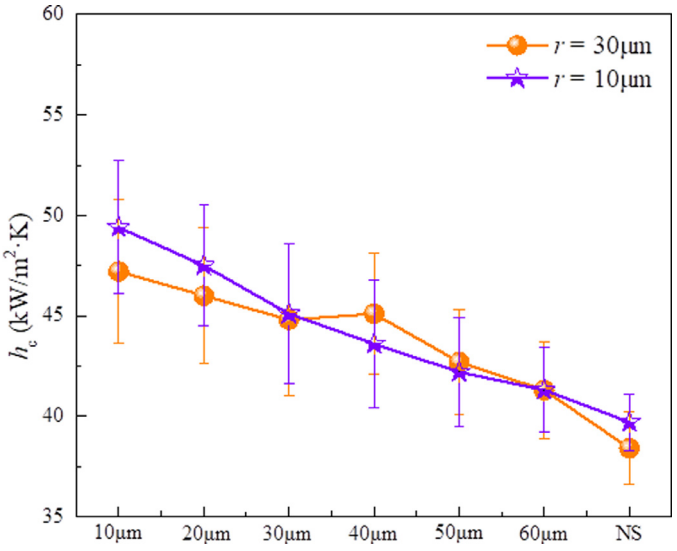

Fig. 8. Variation of the heat transfer coefficient with micropillar spacing at $\Delta T = 1.0$ K .

croscopic mechanism underlying the dynamic evolution of condensate droplets on the micropillared surface at different subcooling degrees is still poorly understood. To reveal the mechanism of droplet evolution at the various subcoolings, the dynamic behaviors of condensate droplets on the S40R30 surface at different subcoolings is shown in Figs. 9(a-c). At the subcooling of 0.5 K (Fig. 9a), the droplets nucleate randomly at the top, side and valley of micropillars. Although the smaller droplets are observed to coalesce at the top and valley micropillars, the maximal droplet size is smaller than the micropillar size for a long operating time. As the condensation proceeds, the thermal resistance of the droplets is already large when they grow to the same size as micropillars. The condensation rate becomes smaller and smaller and the condensing system is in the quasi-equilibrium state. As the surface subcooling increases to 4.0 K (Fig. 9b), the droplets merge to cover some micropillars, forming the liquid bridges between micropillars. Notably, due to the great thermal resistance of accumulated droplets, the condensation is extremely low after operating 40 min or even 1 h. And the condensate exists in the form of discrete droplets rather than a continuous liquid film.

When the subcooling is sufficiently high ($\Delta T = 12.0$ K, Fig. 9c), the overgrown droplets excess the removed droplets, resulting in the flood condensation. Eventually, a thin liquid film is formed on the substrate. Note that, the thickness of liquid film is in the same order of magnitude as the height of micropillars, thus maintaining the superior heat transfer over filmwise condensation. It can be seen from Fig. 10 at a lower 600 × magnification that the condensate droplets first spread over the top of micropillars (dark gray to light gray). Then, condensate droplets grow and merge to fill the micropillar gaps, thereby forming a liquid film. Note that, the liquid film does not flood the top of all the micropillar arrays. Due to the absence of nanostructures on the sides of micropillars, the surface wettability is much stronger over that of the top and bottom of micropillars. After condensing into a liquid film, the condensate at the top is removed, maintaining a thin film on the substrate. The thickness of liquid film is the same order of magnitude as the height of the micropillar (from 70 s to 107 s). The thermal resistance caused by the thickness of liquid layer is reduced, thus enhancing the heat transfer performance. Details of ESEM observations can be found in Supporting Information S4. According to the nucleation theory [50], the nucleation density increases significantly as the surface subcooling rises. The condensate floods the cooled substrate, thereby leading to the transition from dropwise condensation to filmwise condensation. However, the condensate on the top of micropillars is sucked into the gaps, leading to a thin liquid layer as high as the micropillars.

Figs. 9(d-e) show the variation of heat flux q and heat transfer coefficient h_c versus the surface subcooling. The q and h_c are the average values obtained from 5 repeated tests, and the corresponding error bars are calculated from the standard derivations. The hydrophobic NS is used as a reference surface for comparison. The green diamonds denote the q and h_c of the NS, the gray squares is the predicted values of Nusselt theory. At a lower surface subcooling, the q and h_c of the NS are higher than the theoretical values; however, as the subcooling is large enough (ΔT ~ 25 K), the q and h_c of the NS are reduced to be equal to the Nusselt values because of the completely filmwise condensation on the NS. The orange circles, purple triangles and pink inverted triangles represent the q and h_c of the S10R30, S30R30 and S60R30 surface, respectively. We can see that the heat flux q displays an increasing trend with the increase of surface subcooling. Furthermore, smaller micropillar spacing provides the superior heat transfer performance. As the surface subcooling is approximately 25 K, the heat flux of S10R30, S30R30 and S60R30 surfaces is enhanced by 30.9%, 22.1%, and 12.5% respectively, compared to that of the NS. Obviously, the condensation heat transfer coefficient h_c is higher after adding the micropillar arrays. At a lower subcooling, a higher HTC is maintained on both nanostructured and microstructured surfaces. As the subcooling further increases, a relatively higher HTC can be maintained on the micropillared surface despite the filmwise condensation. The liquid film formed on the NS reaches hundreds of micrometers or even a few millimetres thick. The heat transfer efficiency is quite poor due to the thermal resistance of thick liquid layer. In contrast, the liquid layer is limited by micropillar arrays, the thickness of which is nearly the same as the height of micropillars. The microstructured surface maintains a high HTC despite the fact that the liquid film covers the whole substrate (See Supporting Information S5). The experimental results indicate that the condensation HTC of S10R30, S30R30 and S60R30 surface is enhanced by 26.4%, 20.7% and 9.9% over the NS surface at the subcooling of ~25 K.

4.4. LB simulations of condensation heat transfer

Although the dynamic behaviors of condensate droplets and the overall heat transfer performance on the different microstructured surfaces are experimentally investigated, the microdroplet dynamics cannot be captured due to the limitations of high-speed camera magnification. In addition, the flow field and temperature field caused by the microdroplet movement are poorly understood. Therefore, a microscopic numerical method is urgently needed to further study the condensation heat transfer on the microstructured surfaces in microscale. Figs. 11(a-d) show four typical condensation behaviors observed on the different surfaces. The droplets randomly nucleate and grow on the NS with extremely inhomogeneous size distribution. Three-phase contact lines of the larger droplets with the irregular shapes show that a portion of droplets have penetrated into the nanostructures (Fig. 11a). For the S20R10 surface with smaller spacing, a thin liquid film completely covers the micropillars. As the spacing increases, it is observed on the S40R10 surface that the droplets at the valley of micropillars first expand to contact the surrounding micropillars and then grow upward squeezed by the micropillars, while the droplets at the top of pillars freely. On the contrary, the droplets on the S60R10 surface prefer to cover the individual micropillars rather than filling the gaps.

Figs. 11(e-h) give the LB simulations of microdroplet nucleation and growth on the different surfaces. First of all, two tests are

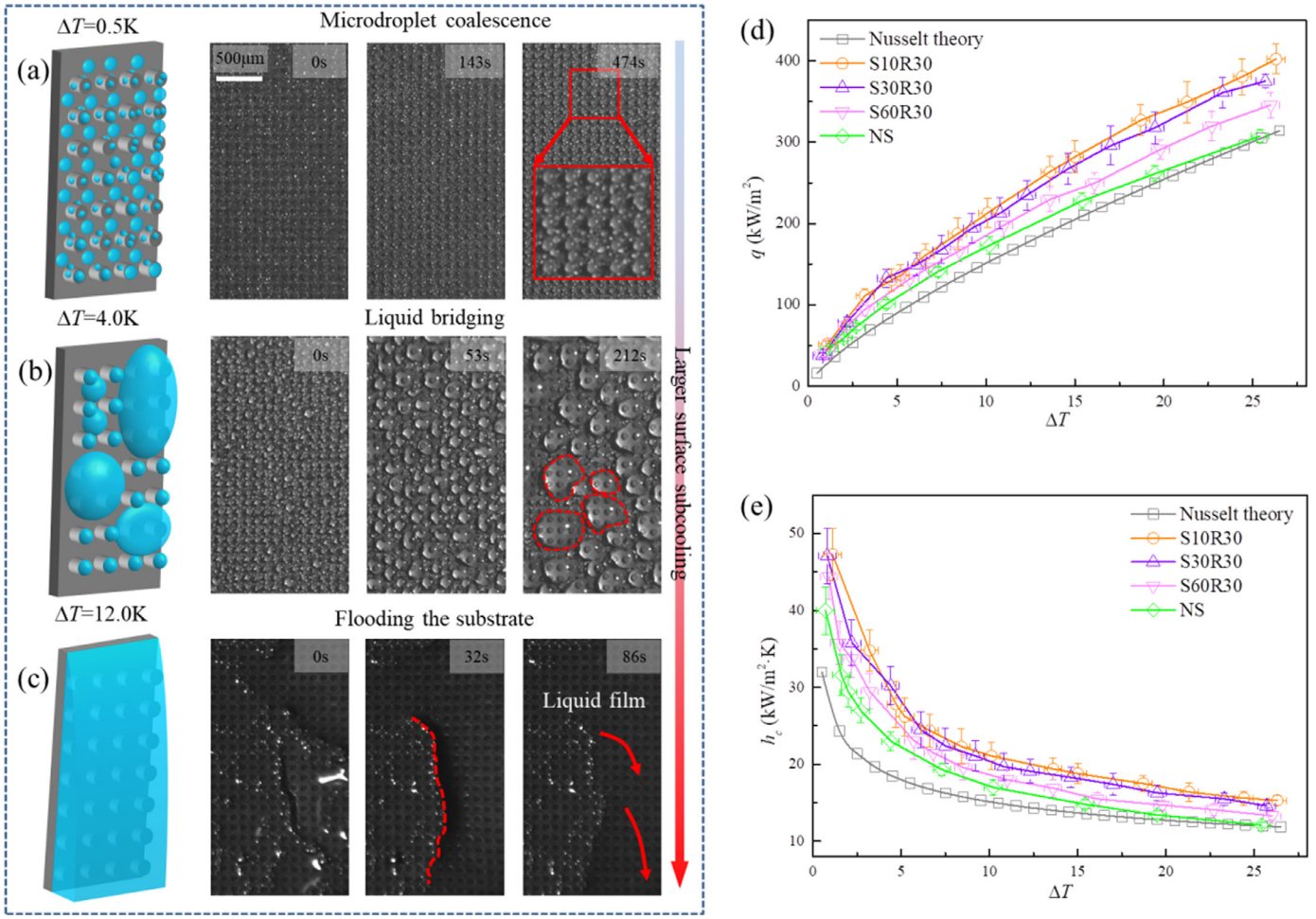

Fig. 9. (a-c) Dynamic evolution of condensate droplets at the different subcoolings; Variation of (d) heat flux and (e) heat transfer coefficient versus the surface subcooling.

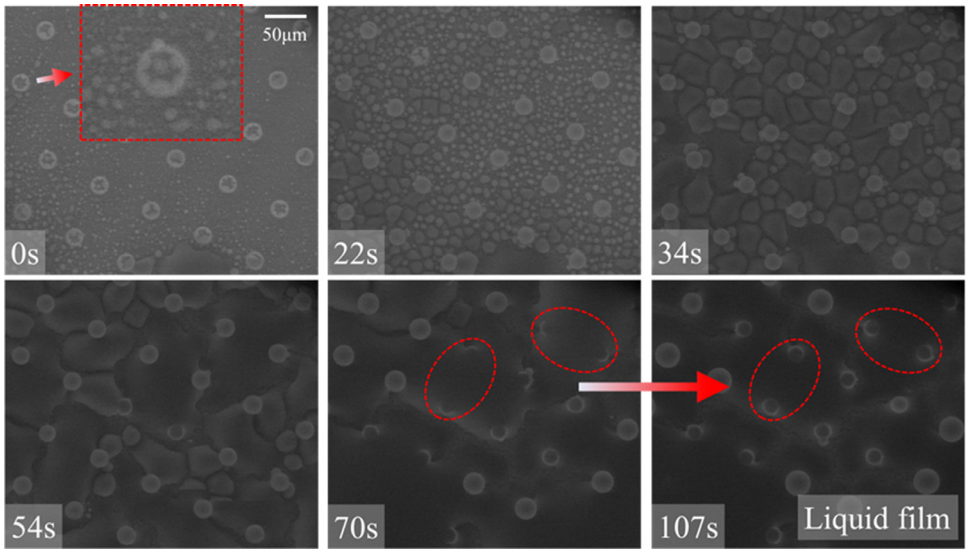

Fig. 10. The top view of condensate dynamics observed by ESEM (600 × magnification) .

applied to check the applicability of LB phase change model for simulating the condensation heat transfer (See Supporting Information S6). Due to the limitations of grid structure, the nanostructures in the LB simulations are neglected. In this section, we concentrate on the microdroplet growth and coalescence on the micropillared surfaces. To ensure the same surface wettability, the contact angle on the smooth surface (135.6°) in simulation is almost the same as that on the NS (135.2°). For the micropillared surface, the wettability of the side pillars (114.0°) is stronger than that of the top and bottom (135.6°), which is consistent with the experimental results. In the meantime, the width and height of micropillars ($2r = 20\ \mu$m, $h = 25\ \mu$m) are the same as those of sil-

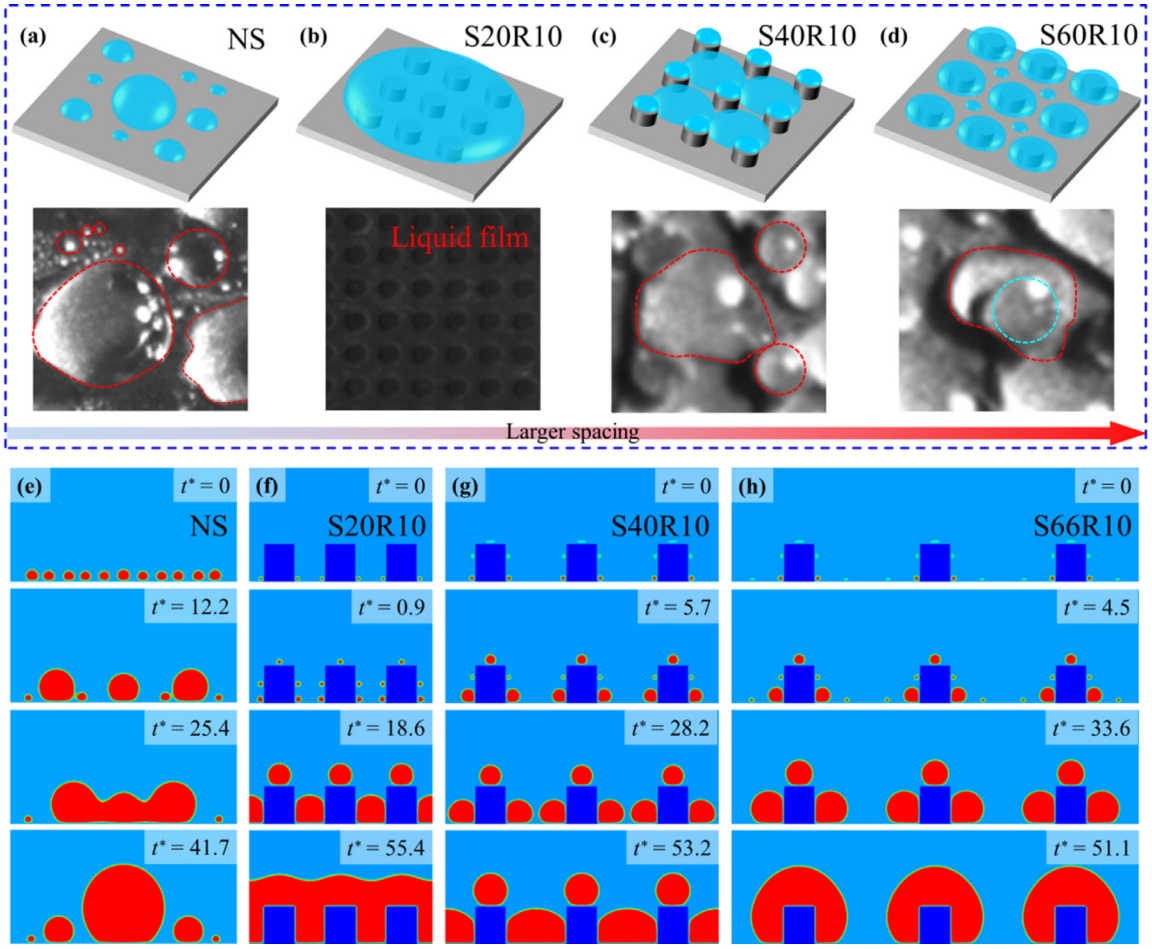

Fig. 11. Four typical condensate behaviors in experiments: (a) conventional dropwise condensation; (b) filmwise condensation on the S20R10 surface; (c) droplets merging to fill the gaps on the S40R10 and (d) droplet merging to enclose the entire micropillar on the S60R10 surface. LB simulations of condensation heat transfer on the (e) smooth surface, (f) S20R10, (g) S40R10 and (h) S66R10 surface. .

icon samples in experiments. As shown in Fig. 11(e), the condensate droplets first nucleate uniformly on the smooth hydrophobic substrate. The droplets with different sizes are formed after the continuous coalescence, and the size distribution corresponds to NS in Fig. 11(a). For the S20R10 surface (Fig. 11f), the condensate microdroplets preferentially nucleate at the bottom corner of micropillars. As can be seen from the images of ESEM observations at 2400 × magnification, the condensed droplets preferentially nucleate at the bottom corner of the micropillars (See Supporting Information S4). Subsequently, three extra nucleation sites appear on each pillar. As the condensation proceeds, the droplets coalesce to the larger ones at the top and bottom corner of pillars. After the bottom gaps are filled, the droplets grow upward squeezed by the micropillars. Finally, the liquid film completely floods the micropillars, which agrees well with the experimental observations on the S20R10 surface. For the S40R10 surface (Fig. 11g), the droplets merge with each other at the gaps of micropillars without exceeding the height of micropillars. In addition, the droplets at the corners merge to the large ones with the help of other bottom nucleation sites, thus filling the gaps between micropillars, which correspond to the observations in Fig. 11(c). When the spacing is large enough (Fig. 11h), the droplets grow and coalesce on the substrate as expected. However, the bottom droplets first merge with the top ones to cover the single micropillar rather than coalescing to fill the gaps. The dynamic behaviors of droplets agree well with the observations in Fig. 11(d). The influence of micropillar spacing on the droplet behaviors from a microscopic perspective is further elucidated via comparing the LB simulations of four typical droplet behaviors with the experimental observations. Note that, the ratio of micropillar spacing to width in simulations (Fig. 11h) is slightly greater than that in experiments (Fig. 11d). This is because the influence of nanostructures on the condensate dynamics in the LB simulations is neglected. In addition, condensate droplets on the surface of S40R10 and S66R10 eventually merge into a liquid film because condensate cannot be removed in a closed system in LB simulations. Overall, the droplet behaviors in the LB simulations agree well with the experimental observations.

In order to further understand the droplet nucleation, growth and coalescence on the micropillared surface in microscale, evolution of the streamlines in the process of condensation is presented in Fig. 12. Initially ($t^* = 1.2$), the steam flows to the bottom corners of micropillars and two counter rotating vortexes are generated at the corners. Therefore, the droplets prefer to nucleate at the bottom corners. Subsequently, the more rotating vortexes appear at the top and sides of micropillars, which means that the nucleation sites are increased. As the condensation proceeds ($t^* = 3.6$), the droplets begin to merge with each other, which can be reflected from the rotating vortexes near the droplet interfaces. Finally, the droplets at the corners expand laterally, indicating the occurrence of droplet merging in the gaps ($t^* = 5.6$).

It can be seen from the temperature distributions in Fig. 13 that a thick heat transfer layer exists at the gas-solid contact area before nucleation. As the droplets first nucleate at the corners, the steam condenses into the liquid and release the latent heat

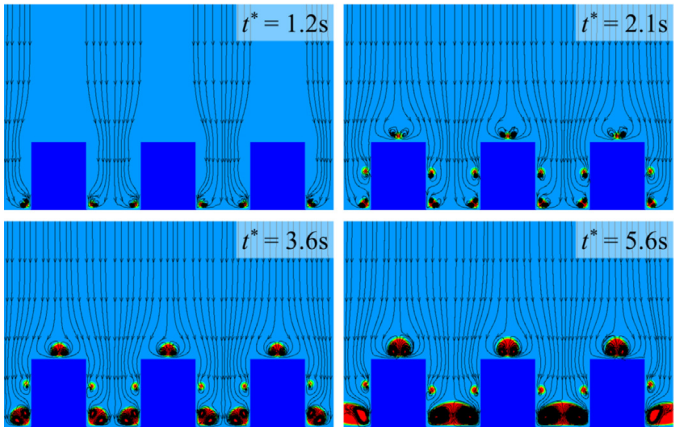

Fig. 12. Evolution of streamlines in the process of condensation on the S20R10 surface. .

of phase change. At this time ($t^* = 2.1$), the temperature inside the droplets is slightly higher than the temperature of heat transfer layer without phase change. In addition, it is found that the temperature of droplets is risen before and after the coalescence, which may be due to releasing the surface energy after coalescence. As the droplets grow and merge, the temperature of bottom droplets is lower than that of the top droplets.

In order to further reveal the microscopic mechanisms of condensation heat transfer on the different micropillared surfaces, variation of average heat flux versus time at the various spacing is analysed. The average heat flux is calculated according to the Fourier's law: $q = -\lambda(\partial T/\partial y)_{y=0}$ (The detailed information of heat flux can refer to our previous work [51].). Since the change of heat flux versus time is rather complex, a few typical examples are chosen for detailed analysis. Fig. 14 shows the evolution of heat flux with time on three different micropillared surfaces at the beginning of condensation. Pink squares, green circles and blue triangles represent the heat flux of S20R10, S40R10 and S66R10 surfaces, respectively. During the initial nucleation stage, the heat flux increases sharply. For the case of S66R10 surface, the number of nucleation sites is increased from 6 at the bottom corners to 21 over the entire substrate (e.g., image G shows the nucleation process of droplets). As is shown in Fig. 13, the thickness of the subcooled steam layer is reduced and the temperature gradient near the substrate becomes larger in the process of nucleation. In addition, the change from gas-solid heat transfer to efficient liquid-solid heat transfer at the nucleation sites leads to a dramatic increase in heat flux, which agrees well with the Amir and Ali's results [52]. As the condensation proceeds, the heat flux decreases gradually and exhibits random fluctuations over time, which is caused by the growth and coalescence of several droplets (images H-I). The heat flux fluctuates more sharply, especially for the S20R10 micropillared surface. As can be seen from images A-C, the droplets at the sides of micropillars undergo the nucleation, growth and after being absorbed by the larger ones at the corners, accompanied by an increase and then decrease in heat flux with time. And the similar regular fluctuations in heat flux occur during the following condensation.

For the three typical dynamic behaviors of condensate droplets on the micropillared surfaces in Figs. 11(b-d, f-h), variation of the heat flux versus time is plotted in Fig. S8. For the S20R10 surface (Fig. S10a), the droplets at the upper of micropillars are continuously engulfed by the larger ones between micropillars after completely filling the gaps, resulting in the relatively ordered fluctuations in heat flux. As the droplets merge to form a liquid film, the heat flux decreases over 35%. For the S40R10 surface (Fig. S10b), when the droplets at the sides of micropillars grow to merge with the top droplets, the heat flux decreases with time. Then, the top droplets are dragged away, improving the heat flux. After the larger droplets merge to fill the gaps, the heat flux decreases dramatically because of the increased liquid-solid contact area. For the

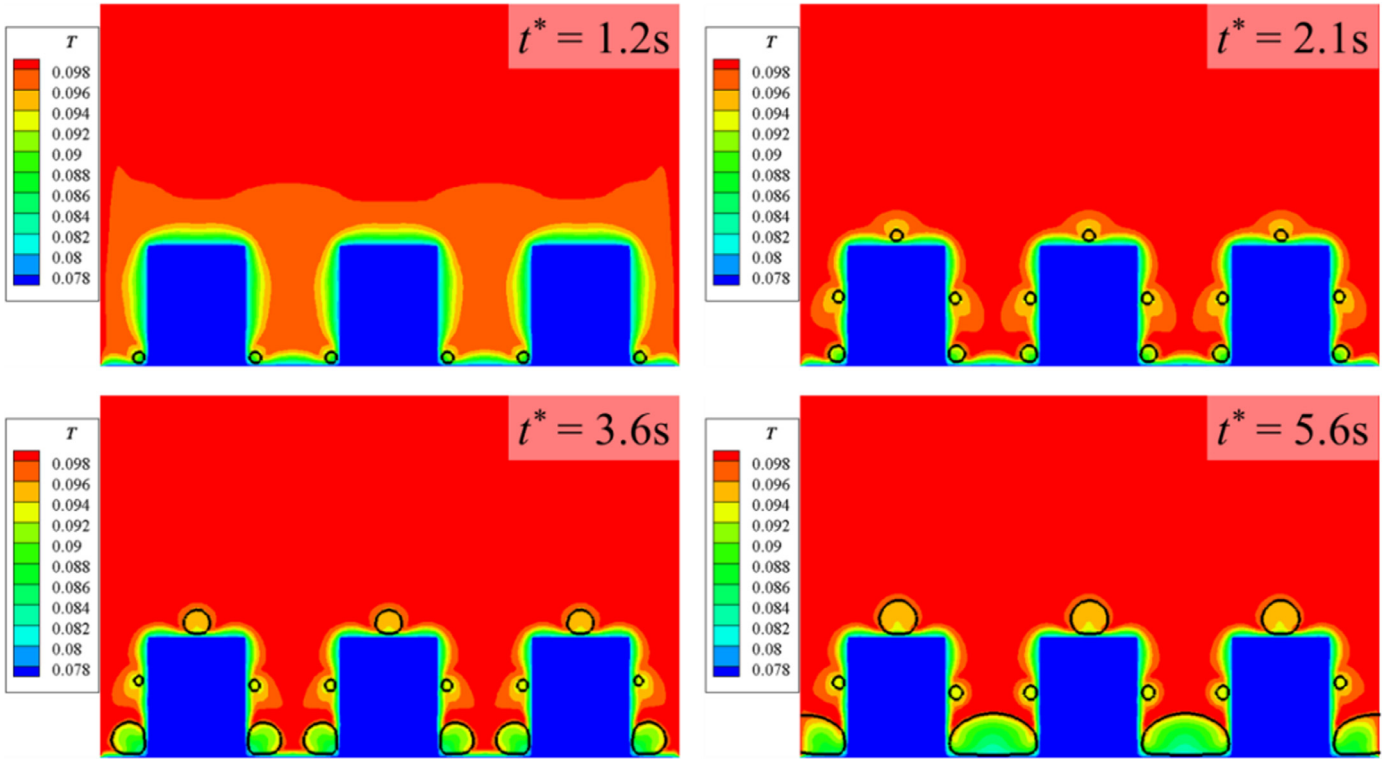

Fig. 13. Temperature distribution in the process of condensation on the S20R10 surface. .

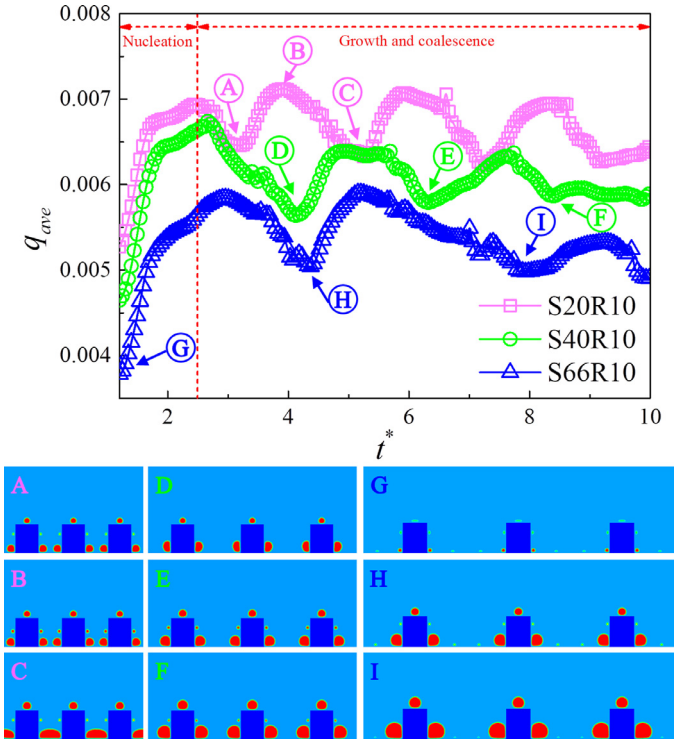

Fig. 14. Variation of the heat flux versus time on the micropillared surfaces with different spacing in the initial stage of condensation.

S66R10 surface (Fig. S10c), the coalescence of droplets at the sides of micropillars leads to the decrease heat flux. Finally, the growing droplets merge to enclose the whole micropillar, the heat flux decreases again. To sum up, all three typical condensate behaviors, involving dropwise condensation transition to filmwise condensation, merging to fill the micropillar gaps and coalescing to enclose the whole micropillar, result in a significant decrease in heat flux.

5. Conclusions

To sum up, the effects of micropillar spacing and surface subcooling on the dynamic behavior of condensate droplets and condensation heat transfer performance on the micropillared and nanopillared surfaces have been experimentally and numerically studied. The larger micropillar spacing can worsen the heat transfer efficiency. Moreover, at large subcoolings (~25 K), the condensate film covers the micropillar arrays, resulting in the flood condensation. Surprisingly, the microscopic ESEM observations show that the thickness of condensate layer is the same order of magnitude as the height of micropillars. The heat transfer coefficient of S10R30 surface is enhanced by 26.4% compared to the nanostructured surface, which demonstrates the superior condensation heat transfer performance of the superhydrophobic surfaces composed of nanopillars and micropillars. Concluded from the LB simulations and ESEM observations, the condensate droplets first nucleate at the bottom corner of micropillars. In addition, the condensate droplets merge to form a film, fill the micropillar gaps, and cover the entire micropillars, resulting in a sharp decrease in heat flux. This work provides insights into the design of micro- and nano-structured surfaces for further enhancing heat transfer.

Credit author statement

Xin Wang: Conceptualization, Methodology, Validation, Formal analysis, Investigation, Data curation, Writing original draft, Visualization, Writing review & editing.

Bo Xu: Conceptualization, Methodology, Software, Validation, Formal analysis, Funding acquisition, Investigation, Visualization.

Qiusheng Liu: Conceptualization, Methodology, Formal analysis, Funding acquisition, Investigation.

Yang Yang: Conceptualization, Funding acquisition, Investigation.

Zhenqian Chen: Conceptualization, Supervision, Funding acquisition, Project administration, Writing review & editing.

Declaration of Competing Interest

The authors declare that they have no known competing financial interests or personal relationships that could have appeared to influence the work reported in this paper.

Acknowledgments

This work was supported by National Natural Science Foundation of China (No.52006031), ESA-CMSA International Cooperation of Space Experiment Project (Study on Condensation and Enhancement Methods under Microgravity) and the Scientific Research Foundation of Graduate School of Southeast University (YBPY1949).

Supplementary materials

Supplementary material associated with this article can be found, in the online version, at doi:10.1016/j.ijheatmasstransfer.2021.121526.

References

[1] L.L. Vasiliev, Heat pipes in modern heat exchangers, Appl. Therm. Eng. 25 (2005) 1–19.
[2] H.J. Cho, D.J. Preston, Y. Zhu, E.N. Wang, Nanoengineered materials for liquid–vapour phase-change heat transfer, Nat. Rev. Mater. 2 (2017) 16092.
[3] C. Li, C. Yu, S. Zhou, Z. Dong, L. Jiang, Liquid harvesting and transport on multiscaled curvatures, Proc. Natl. Acad. Sci. U.S.A. 117 (2020) 23436–23442.
[4] T. Xu, Y. Lin, M. Zhang, W. Shi, Y. Zheng, High-efficiency fog collector: water unidirectional transport on heterogeneous rough conical wires, ACS Nano 10 (2016) 10681–10688.
[5] J. Lei, Z. Guo, A fog-collecting surface mimicking the Namib beetle: its water collection efficiency and influencing factors, Nanoscale 12 (2020) 6921–6936.
[6] D. Li, C. Qian, S. Gao, X. Zhao, Y. Zhou, Self-propelled drop jumping during defrosting and drainage characteristic of frost melt water from inclined superhydrophobic surface, Int. J. Refrigr. 79 (2017) 25–38.
[7] X. Ji, J. Xu, H. Li, G. Huang, Switchable heat transfer mechanisms of nucleation and convection by wettability match of evaporator and condenser for heat pipes: nanostructured surface effect, Nano Energy 38 (2017) 313–325.
[8] T. Fujii, H. Uehara, C. Kurata, Laminar filmwise condensation of flowing vapour on a horizontal cylinder, Int. J. Heat Mass Tran. 15 (1972) 235–246.
[9] P. Liu, J. Ho, T.N. Wong, K.C. Toh, Convective filmwise condensation on the outer surface of a vertical tube: a theoretical analysis, Int. J. Heat Mass Tran. 161 (2020) 120266.
[10] Y. Hou, M. Yu, X. Chen, Z. Wang, S. Yao, Recurrent filmwise and dropwise condensation on a beetle mimetic surface, ACS Nano 9 (2015) 71–81.
[11] E. Olceroglu, M. McCarthy, Self-organization of microscale condensate for delayed flooding of nanostructured superhydrophobic surfaces, ACS Appl. Mater. Interfaces 8 (2016) 5729–5736.
[12] A. Ghosh, S. Beaini, B.J. Zhang, R. Ganguly, C.M. Megaridis, Enhancing dropwise condensation through bioinspired wettability patterning, Langmuir 30 (2014) 13103–13115.
[13] Y. Shang, Y. Hou, M. Yu, S. Yao, Modeling and optimization of condensation heat transfer at biphilic interface, Int. J. Heat Mass Tran. 122 (2018) 117–127.
[14] S. Feng, J. Delannoy, A. Malod, H. Zheng, D. Quéré, Z. Wang, Tip-induced flipping of droplets on Janus pillars: from local reconfiguration to global transport, Sci. Adv. 6 (2020) eabb4540.
[15] R. Wen, Z. Lan, B. Peng, W. Xu, R. Yang, X. Ma, Wetting transition of condensed droplets on nanostructured superhydrophobic surfaces: coordination of surface properties and condensing conditions, ACS Appl. Mater. Interfaces 9 (2017) 13770–13777.
[16] N. Miljkovic, R. Enright, E.N. Wang, Effect of droplet morphology on growth dynamics and heat transfer during condensation on superhydrophobic nanostructured surfaces, ACS Nano 6 (2012) 1776–1785.
[17] R. Mukherjee, A.S. Berrier, K.R. Murphy, J.R. Vieitez, J.B. Boreyko, How surface orientation affects jumping-droplet condensation, Joule 3 (2019) 1360–1376.
[18] X. Yan, L.C. Zhang, S. Sett, L.Z. Feng, C.Y. Zhao, Z.Y. Huang, H. Vahabi, A.K. Kota, F. Chen, N. Miljkovic, Droplet jumping: effects of droplet size, surface structure, pinning, and liquid properties, ACS Nano 13 (2019) 1309–1323.

[19] P. Zhang, Y. Maeda, F. Lv, Y. Takata, D. Orejon, Enhanced coalescence-induced droplet-jumping on nanostructured superhydrophobic surfaces in the absence of microstructures, ACS Appl. Mater. Interfaces 9 (2017) 35391–35403.
[20] X. Chen, J. Wu, R. Ma, M. Hua, N. Koratkar, S. Yao, Z. Wang, Nanograssed micropyramidal architectures for continuous dropwise condensation, Adv. Funct. Mater. 21 (2011) 4617–4623.
[21] G. Zhao, G. Zou, W. Wang, R. Geng, X. Yan, Z. He, L. Liu, X. Zhou, J. Lv, J. Wang, Competing effects between condensation and self-removal of water droplets determine antifrosting performance of superhydrophobic surfaces, ACS Appl. Mater. Interfaces 12 (2020) 7805–7814.
[22] C.W. Lo, Y.C. Chu, M.H. Yen, M.C. Lu, Enhancing condensation heat transfer on three-dimensional hybrid surfaces, Joule 3 (2019) 2806–2823.
[23] X. Yan, F. Chen, S. Sett, S. Chavan, H. Li, L. Feng, L. Li, F. Zhao, C. Zhao, Z. Huang, N. Miljkovic, Hierarchical condensation, ACS Nano 13 (2019) 8169–8184.
[24] X. Chen, R.S. Patel, J.A. Weibel, S.V. Garimella, Coalescence-induced jumping of multiple condensate droplets on hierarchical superhydrophobic surfaces, Sci. Rep. 6 (2016) 18649.
[25] J.B. Boreyko, C.H. Chen, Self-propelled dropwise condensate on superhydrophobic surfaces, Phys. Rev. Lett. 103 (2009) 184501.
[26] M.D. Mulroe, B.R. Srijanto, S.F. Ahmadi, C.P. Collier, J.B. Boreyko, Tuning superhydrophobic nanostructures to enhance jumping-droplet condensation, ACS Nano 11 (2017) 8499–8510.
[27] R. Wen, S. Xu, X. Ma, Y.C. Lee, R. Yang, Three-dimensional superhydrophobic nanowire networks for enhancing condensation heat transfer, Joule 2 (2018) 269–279.
[28] C. Lv, P. Hao, X. Zhang, F. He, Dewetting transitions of dropwise condensation on nanotexture-enhanced superhydrophobic surfaces, ACS Nano 9 (2015) 12311–12315.
[29] N. Miljkovic, R. Enright, Y. Nam, K. Lopez, N. Dou, J. Sack, E.N. Wang, Jumping–droplet-enhanced condensation on scalable superhydrophobic nanostructured surfaces, Nano Lett 13 (2013) 179–187.
[30] R. Wen, S. Xu, D. Zhao, Y.C. Lee, X. Ma, R. Yang, Hierarchical superhydrophobic surfaces with micropatterned nanowire arrays for high-efficiency jumping droplet condensation, ACS Appl. Mater. Interfaces 9 (2017) 44911–44921.
[31] D. Orejona, O. Shardt, N.S.K. Gunda, T. Ikuta, K. Takahashi, Y. Takata, S.K. Mitra, Simultaneous dropwise and filmwise condensation on hydrophilic microstructured surfaces, Int. J. Heat Mass Tran. 114 (2017) 187–197.
[32] J. Xie, J. Xu, X. Li, H. Liu, Dropwise condensation on superhydrophobic nanostructure surface, Part I: long-term operation and nanostructure failure, Int. J. Heat Mass Tran. 129 (2019) 86–95.
[33] Q. Li, K. Luo, Q. Kang, Y. He, Q. Chen, Q. Liu, Lattice Boltzmann methods for multiphase flow and phase-change heat transfer, Prog. Energ. Combust. 52 (2016) 62–105.
[34] L. Chen, Q. Kang, Y. Mu, Y. He, W. Tao, A critical review of the pseudopotential multiphase lattice Boltzmann model: methods and applications, Int. J. Heat Mass Tran. 76 (2014) 210–236.
[35] X. Liu, P. Cheng, Lattice Boltzmann simulation of steady laminar film condensation on a vertical hydrophilic subcooled flat plate, Int. J. Heat Mass Tran. 62 (2013) 507–514.
[36] X. Liu, P. Cheng, Lattice Boltzmann simulation of steady laminar film condensation on a vertical hydrophilic subcooled flat plate, Int. J. Heat Mass Tran. 64 (2013) 1041–1052.
[37] X. Li, P. Cheng, Lattice Boltzmann simulations for transition from dropwise to filmwise condensation on hydrophobic surfaces with hydrophilic spots, Int. J. Heat Mass Tran. 110 (2017) 710–722.
[38] Q. Guo, P. Cheng, 3D lattice Boltzmann investigation of nucleation sites and dropwise-to-filmwise transition in the presence of a non-condensable gas on a biomimetic surface, Int. J. Heat Mass Tran. 128 (2019) 185–198.
[39] L. Shen, G. Tang, Q. Li, Y. Shi, Hybrid wettability-induced heat transfer enhancement for condensation with noncondensable gas, Langmuir 35 (2019) 9430–9440.
[40] Y. Shi, G. Tang, L. Shen, Study of coalescence-induced droplet jumping during phase-change process in the presence of noncondensable gas, Int. J. Heat Mass Tran. 152 (2020) 119506.
[41] R.J. Moffat, Describing the uncertainties in experimental results, Exp. Therm. Fluid Sci. 1 (1) (1988) 3–17.
[42] Q. Li, Q. Kang, M.M. Francois, Y. He, K. Luo, Lattice Boltzmann modeling of boiling heat transfer: the boiling curve and the effects of wettability, Int. J. Heat Mass Tran. 85 (2015) 787–796.
[43] Q. Li, K. Luo, X. Li, Lattice Boltzmann modeling of multiphase flows at large density ratio with an improved pseudopotential model, Phys. Rev. E 87 (2013) 053301.
[44] P. Lallemand, L. Luo, Theory of the lattice Boltzmann method: dispersion, dissipation, isotropy, Galilean invariance, and stability, Phys. Rev. E 61 (2000) 6546–6562.
[45] P. Yuan, L. Schaefer, Equations of state in a lattice Boltzmann model, Phys. Fluids 18 (2006) 042101.
[46] X. Wang, B. Xu, Z. Chen, Y. Yang, Q. Cao, Lattice Boltzmann modeling of condensation heat transfer on downward-facing surfaces with different wettabilities, Langmuir 36 (2020) 9204–9214.
[47] Q. Zou, X. He, On pressure and velocity boundary conditions for the lattice Boltzmann BGK model, Phys. Fluids 9 (1997) 1591–1598.
[48] A.B.D. Cassie, S. Baxter, Wettability of porous surfaces, Trans. Faraday Soc. 40 (1944) 546–550.
[49] N. Miljkovic, R. Enright, E.N. Wang, Modeling and optimization of superhydrophobic condensation, J. Heat Trans-T ASME 135 (2013) 111004.
[50] A. Dillmann, G.E.A. Meier, A Refined Droplet Approach to the Problem of Homogeneous Nucleation from the Vapor-Phase, J. Chem. Phys. 94 (1991) 3872–3884.
[51] X. Wang, B. Xu, Z. Chen, Y. Yang, Q. Cao, Lattice Boltzmann simulation of dropwise condensation on the microstructured surfaces with different wettability and morphologies, Int. J. Therm. Sci. 160 (2021) 106643.
[52] A. Amir, M. Ali, Droplet condensation on chemically homogeneous and heterogeneous surfaces, J. Appl. Phys. 120 (2016) 124901.